

Artificial Muscles

Applications of Advanced Polymeric Nanocomposites

Mohsen Shahinpoor
School of Engineering and School of Medicine
University of New Mexico
Albuquerque, New Mexico, USA

Kwang J. Kim
College of Engineering
University of Nevada-Reno
Reno, Nevada, USA

Mehran Mojarad
Pharmaceutical Delivery Systems
Eli Lilly & Company
Indianapolis, Indiana, USA



Taylor & Francis

Taylor & Francis Group

New York London

Taylor & Francis is an imprint of the
Taylor & Francis Group, an informa business

CRC Press
Taylor & Francis Group
6000 Broken Sound Parkway NW, Suite 300
Boca Raton, FL 33487-2742

© 2007 by Taylor & Francis Group, LLC
CRC Press is an imprint of Taylor & Francis Group, an Informa business

No claim to original U.S. Government works
Printed in the United States of America on acid-free paper
10 9 8 7 6 5 4 3 2 1

International Standard Book Number-10: 1-58488-713-3 (Hardcover)
International Standard Book Number-13: 978-1-58488-713-3 (Hardcover)

This book contains information obtained from authentic and highly regarded sources. Reprinted material is quoted with permission, and sources are indicated. A wide variety of references are listed. Reasonable efforts have been made to publish reliable data and information, but the author and the publisher cannot assume responsibility for the validity of all materials or for the consequences of their use.

No part of this book may be reprinted, reproduced, transmitted, or utilized in any form by any electronic, mechanical, or other means, now known or hereafter invented, including photocopying, microfilming, and recording, or in any information storage or retrieval system, without written permission from the publishers.

For permission to photocopy or use material electronically from this work, please access www.copyright.com (<http://www.copyright.com/>) or contact the Copyright Clearance Center, Inc. (CCC) 222 Rosewood Drive, Danvers, MA 01923, 978-750-8400. CCC is a not-for-profit organization that provides licenses and registration for a variety of users. For organizations that have been granted a photocopy license by the CCC, a separate system of payment has been arranged.

Trademark Notice: Product or corporate names may be trademarks or registered trademarks, and are used only for identification and explanation without intent to infringe.

Library of Congress Cataloging-in-Publication Data

Shahinpoor, Mohsen.

Artificial muscles : applications of advanced polymeric nanocomposites / Mohsen Shahinpoor, Kwang J. Kim, Mehran Mojarad.

p. ; cm.

Includes bibliographical references and index.

ISBN-13: 978-1-58488-713-3 (hardcover : alk. paper)

ISBN-10: 1-58488-713-3 (hardcover : alk. paper)

1. Nanotechnology. 2. Muscles. 3. Artificial organs. 4. Biomimetic polymers. I. Kim, Kwang J. II. Mojarad, Mehran. III. Title.

[DNLN: 1. Polymers--chemistry. 2. Artificial Organs. 3. Biomimetic Materials. 4. Electrophysiology--methods. 5. Muscles--physiology. 6. Nanostructures. QT 37.5.P7 S525a 2007]

TP248.25.N35S53 2007
621.4--dc22

2006027040

Visit the Taylor & Francis Web site at
<http://www.taylorandfrancis.com>

and the CRC Press Web site at
<http://www.crcpress.com>

Prologue

In this book, thorough reviews of existing knowledge in connection with ionic polymeric conductor nanocomposites (IPCNCs)—including ionic polymeric metal nanocomposites (IPMNCs) as biomimetic distributed nanosensors, nanoactuators, nanotransducers, nanorobots, artificial muscles, and electrically controllable intelligent polymeric network structures—are presented. Two brief introductory appendices on biological muscles are also presented to offer short reviews of how biological muscles work, how biomimetic actuator materials in general have been developed based on biological muscles, and how the latter are limited in their performance compared with biological muscles. This is intended to help provide motivation to understanding as well as a means of comparison for artificial muscle materials to be discussed and analyzed in this book.

Where possible, comparisons have been made with biological muscles and applications in noiseless, biomimetic marine propulsion and unmanned aerial vehicles (UAVs) and flapping-wing systems using such electroactive polymeric materials. Furthermore, the book introduces and discusses in detail methods of fabrication and manufacturing of several electrically and chemically active ionic polymeric sensors, actuators, and artificial muscles, such as polyacrylonitrile (PAN), poly(2-acrylamido-2-methyl-1-propanesulfonic) acid (PAMPS), and polyacrylic-acid-*bis*-acrylamide (PAAM), as well as a new class of electrically active composite muscles such as IPCNCs or IPMNCs. These discoveries have resulted in seven U.S. patents regarding their fabrication and application capabilities as distributed biomimetic nanoactuators, nanosensors, nanotransducers, nanorobots, and artificial muscles.

In this book, various methods of IPMNC manufacturing and fabrication are reported. In addition, manufacturing and characterization of PAN muscles are discussed. Conversion of chemical activation to electrical activation of artificial muscles using chemical plating techniques is described. Furthermore, other methodologies, such as physical/chemical vapor deposition methods or physical loading of a conductor phase into near boundary of such materials, are briefly discussed. The technologies associated with pH-activated muscles like PAN fibers have also been detailed. Experimental methods are described to characterize contraction, expansion, and bending of various actuators using isometric, isoionic, and isotonic characterization methods.

Several apparatuses for modeling and testing the various artificial muscles have been described to show the viability of application of chemoactive as well as electroactive muscles. Furthermore, fabrication methods of PAN fiber muscles in different configurations (such as spring-loaded fiber bundles, biceps, triceps, ribbon-type muscles, and segmented fiber bundles) to make a variety of biomimetic nanosensors and nanoactuators have been reported here.

Theories, modeling, and numerical simulations associated with ionic polymeric artificial muscles' electrodynamics and chemodynamics have been discussed, analyzed,

and modeled for the manufactured material. The book concludes with an extensive chapter on all current industrial and medical applications of IPMNCs as distributed biomimetic nanosensors, nanoactuators, nanotransducers, nanorobots, and artificial muscles.

Mohsen Shahinpoor
Kwang J. Kim
Mehran Mojarad

The Authors



Mohsen Shahinpoor is the chief scientist and director of biomedical products at Environmental Robots Incorporated. He is a Regents Professor for Life at the University of New Mexico's School of Engineering and School of Medicine, Neurological Surgery Department. He graduated from the Abadan Institute of Technology with a B.Sc. degree in chemical and materials engineering and received his M.Sc. and Ph.D. degrees in mechanical and aerospace engineering from the University of Delaware. Currently, Dr. Shahinpoor is also director of the Artificial Muscles Research Institute (AMRI). He is the former director of the

Intelligent Materials, Structures and Systems Laboratory and the CAD/CAM, CIM and Robotics Laboratories in the University of New Mexico School of Engineering, where he served as chairman of the Mechanical Engineering Department and associate dean of engineering.

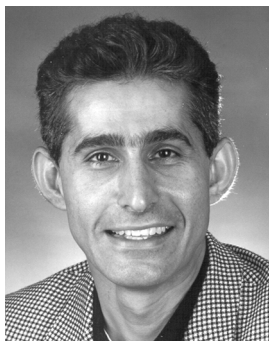
Dr. Shahinpoor has served as principal research scientist at the Johns Hopkins and Northwestern Universities and as visiting professor at the California Institute of Technology. He is a fellow of ASME, fellow of the Institute of Physics (IOP), licensed professional engineer, senior member of SME, and member of the New York Academy of Sciences. Professor Shahinpoor has been involved with the field of intelligent robotic systems for the past 22 years and the field of smart/intelligent materials, structures, and systems for the past 15 years. He has made significant advances in the area of electrically controllable artificial muscles for medical and industrial applications using ionic polymeric metal or conductor nanocomposites, as well as distributed nanosensors, nanoactuators, and artificial muscles. He has produced numerous publications and patents on these subjects.



Kwang J. (Jin) Kim is associate professor in the Mechanical Engineering Department and director of the Active Materials and Processing Laboratory (AMPL) at the University of Nevada, Reno (UNR). He graduated from Yonsei University, Korea, in 1987 and received his M.S. and Ph.D. degrees from Arizona State University in 1989 and 1992, respectively. Later, he completed postdoctoral study at the University of Maryland, College Park (1993–1995). His industrial experience includes senior research engineer at Thermal Electric Devices, Inc. (1995–1997) and chief scientist at Environmental Robots, Inc.

(1997–2001), Albuquerque, New Mexico. From 1996 to 2001, he also was an adjunct professor at University of New Mexico (1996–2001). His research interests are in

active materials/sensors and energy systems. He has authored or coauthored more than 180 technical papers. He is a recipient of the 2006 UNR Lemelson Award for Innovation and Entrepreneurship, the 2002 Ralph E. Powe Junior Faculty Enhancement Award from Oak Ridge Associated Universities, and the 1997 Best Paper Award of ASME/Advanced Energy Systems/HPTC.



Mehran Mojarad is a project management consultant for Eli Lilly and Company, where, as a member of the advanced development team, he has supported development of new devices for large and small molecule drug delivery for a variety of therapeutics markets. Dr. Mojarad is the technical lead in advanced drug delivery technologies including nanotechnology application in targeted drug delivery, transdermal delivery, infusion pumps, injection pens, needle-free injection pens, mucosal delivery, lingual delivery, pulmonary drug delivery, ophthalmic delivery, implants, and MEMS based drug delivery tech-

nologies. He graduated from the University of Maryland, College Park, with a B.S. in mechanical engineering and received his M.S. and Ph.D. degrees in mechanical engineering from the University of New Mexico, Albuquerque.

Dr. Mojarad has more than 18 years of industrial and 6 years of academic research and teaching experience including smart materials, biomimetic robotics, biomedical devices, naval propulsion, semiconductor device manufacturing, and rapid prototyping. He also founded two high-technology materials and robotics companies supporting advanced materials applications in robotics, propulsion, and medical devices. Dr. Mojarad is coauthor of *Ionic Polymer Conductor Composite Artificial Muscles* (ERI/AMRI Press, 2004) and has published more than 13 articles in professional journals. He is a member of ASME, AIAA, SPIE, Sigma Xi, and SVC.

List of Figures

Figure	Description	Page
2.1	Successive photographs of an IPMNC strip showing very large deformation. Samples in (a) and (b) are $1\text{ cm} \times 4\text{ cm} \times 0.2\text{ mm}$, with 2 V; samples in (c) and (d) are $1\text{ cm} \times 8\text{ cm} \times 0.34\text{ mm}$ with 4 V. Note that $\Delta t = 0.5\text{ sec}$ between (a), (b) and (c), (d).	23
2.2(a) and 2.2(b)	Step response displacement characteristics of IPMNC samples. (a) hydrated; (b) semidry.	24
2.2(c)	Displacement characteristics of an IPMNC, ERI-S1. δ : arc length; L_o : effective beam length; $L_o = 1.0\text{ in.}$ (top) and $L_o = 1.5\text{ in.}$ (bottom).	25
2.2(d)	Variation of tip blocking force and the associated deflection if allowed to move versus the applied step voltage for a $1\text{ cm} \times 5\text{ cm} \times 0.3\text{ mm}$ IPMNC Pt-Pd sample in a cantilever configuration.	26
2.3	A typical sensing response of an IPMNC strip of $0.5\text{ cm} \times 2\text{ cm} \times 0.2\text{ mm}$ manually flipped off by about 1 cm tip deflection in a cantilever form and then released.	26
2.4	Perfluorinated sulfonic acid polymers.	27
2.5	Two schematic diagrams showing different electrode penetration and manufacturing processes.	28
2.6	Two SEM micrographs showing the cross-section (left) and close-up (right) of a typical IPMNC.	29
2.7	An atomic force microscopy surface analysis image taken on the functionally graded composite surface electrodes of some typical IPMNCs shown in figure 2.1. The scanned area is $1\text{ }\mu\text{m}^2$. The brighter/darker area corresponds to a peak/valley depth of 50 nm. The surface analysis image has a view angle set at 22° .	30
2.8	TEM micrographs of IPMNC (left: Pt particles; right: a Pt particle).	30
2.9	A schematic of the typical IPMNC and its actuation principle.	31
2.10	Tensile testing results.	32
2.11	A cantilever configuration (left) of the IPMNC (i) and an illustration of positive/negative strains experienced in the operation mode of the IPMNC (ii) in the cathode/anode sides of the electrodes, respectively.	33
2.12	Effect of swelling on the stress-strain characteristics of IPMNCs.	34
2.13	Stiffening of IPMNCs due to placement in an electric field or under electric activation.	34
2.14	The measured AC impedance spectra (magnitude) of IPMNC sample. The moist IPMNC sample has a dimension of 5-mm width, 20-mm length, and 0.2-mm thickness.	35
2.15	A possible equivalent electric circuit of typical IPMNC (top) and measured surface resistance, R_s , as a function of platinum penetration depth (bottom). Note that SEM was used to estimate the penetration depth of platinum in the membrane. The four-probe method was used to measure the surface resistance, R_s , of the IPMNCs. Clearly, the deeper the penetration is, the lower the surface resistance is.	36

Figure	Description	Page
2.16	Steady state current, I , versus applied voltages, E_{app} , on the typical IPMNCs. ERI-K1100 stands for a proprietary IPMNC fabricated by Environmental Robots, Inc. It has a thickness of 2.9 mm and is suitably platinum/gold electroded.	37
2.17	I/V curves for a typical IPMNC. Nafion™-117-based IPMNC.	37
2.18	Frequency dependency of the IPMNC in terms of the normal stress, σ_N , versus the normal strain, ϵ_N , under an imposed step voltage of 1 V. This Nafion-117 IPMNC has a cation of Li ⁺ and a size of 5 × 20 mm.	38
2.19	A schematic illustration of platinum coagulation during the chemical reduction process.	39
2.20(a)	Force response characteristics of the improved IPMNC versus the conventional IPMNC. Note that the improved IPMNC is one treated by an effective dispersing agent.	40
2.20(b)	TEM micrographs of two samples of IPMNC with and without PVP treatment. Note how the addition of polyvinyl pyrrolidone (PVP) causes the nanoparticles of platinum to not coalesce and create a uniform and fairly homogeneous distribution of particles. This is believed to create more uniform internal electric fields and cause the increased force capability of IPMNCs and IPCNCs.	41
2.21(a)	A scanning electron micrograph (SEM) of an IPMNC film sample treated with a dispersing agent polyvinyl pyrrolidone or PVP (top) and its x-ray line scan (bottom). As can be seen, the Pt penetration is deeper, more homogeneous, and more consistent due to the use of the dispersant.	42
2.21(b)	Profiles of platinum concentration versus depth penetration for different diffusivity coefficients D_{eff} . As can be seen, the Pt penetration is deeper, more homogeneous, and more consistent due to use of the dispersant PVP.	42
2.22	Potentiostatic coulometric analyses for the additive treated IPMNC and the conventional IPMNC. This graph shows that an increased current passage (Faraday approach) can contribute to the observed improvement in the force characteristics of IPMNC strips (see fig. 2.19).	43
2.23	Maximum stresses generated by the IPMNCs at given voltages.	44
2.24	Specific energy as a function of frequency for typical IPMNC samples.	45
2.25	Power density output as a function of frequencies.	46
2.26	Thermodynamic efficiency of actuation of the IPMNC as a function of frequency. Nafion-117 was used as a starting material.	47
2.27	Deflection characteristics of IPMNC as a function of time and temperature.	48
2.28	IR thermographs of an IPMNC in action. The hot spot starts from the electrode and propagates toward the tip of the IPMNC strip.	48
2.29	Power consumption of the IPMNC strip bending actuator as a function of activation voltage.	49
2.30	Deflection of the bending IPMNC strip as function of voltage.	49
2.31	Deflection versus current drawn (top) and power input (bottom) at a high pressure of 850 torr and a low pressure of 0.4–1 torr.	49
2.32	IPMNC strip static (V/I) and dynamic (V/I) resistance at various temperatures.	50
2.33	The relation between voltage and current for an IPMNC strip exposed to room temperature = 20 and –100°C.	50
2.34	Venus flytrap (<i>Dionaea muscipula</i>). (a), (b), (c) A plant capable of rapid nastic deployment and movement based on its trigger hair; (d) digital sensing and an IPMNC gold strip (1 cm × 6 cm × 0.3 mm) performing similar rapid closure (e), (f), (g) under a dynamic voltage of 4 V.	52

Figure	Description	Page
2.35	Migration of lithium cations to the surface on the cathode electrode side of a cantilever sample of IPMNC. (a) Sample bent downward, lithium ions appearing on the surface. (b) Sample bent upward with lithium ions disappearing by migration to the other side.	52
2.36	The cation-transport-induced actuation principle of IPMNCs. (a) Before a voltage is applied; (b) after a voltage is applied.	53
2.37	Near-DC sensing data in terms of produced voltages, ΔE , versus displacement. Note that the displacement is shown in terms of the deformed angle relative to standing position in degree in a cantilever configuration. The dimension of the sample sensor is $5 \times 25 \times 0.12$ mm.	54
2.38	Typical voltage/current output of IPMNC samples under flexing/bending. The IPMNC sample has a dimension of 10-mm width, 30-mm length, and 0.3-mm thickness.	55
2.39	Outvoltage due to normal impact of 200-N load on a $2\text{-cm} \times 2\text{-cm} \times 0.2\text{-mm}$ IPMNC sample.	55
2.40	A blocking force measurement configuration.	56
2.41	Two TEM micrographs show the intrinsic platinum particles for an IPMNC mechanically stretched prior to making the metal–ionic polymer composite (left) and with no stretching (right). The 17% uniaxial stretching was performed.	56
2.42	Measured blocking forces (top) and surface resistance of IPMNC samples prepared (bottom). The standard sample size is $5\text{ mm} \times 10\text{ mm} \times 0.2\text{ mm}$. The process information is given in terms of particles used, platinum, and the final material with gold electrodes.	57
2.43	Sequence of events establishing electric shape memory effect. (a) Before the voltage of 4 V is applied to the sample of $10 \times 80 \times 0.34$ mm; (b) 4 sec after the voltage is applied; (c) 6 sec after the electrodes are shorted by connecting the lead wires together; (d) 4 sec later after the same voltage is applied again; (e) 10 min later after the muscle is completely detached from the electrodes with permanent deformation and laid on a table.	59
3.1	Styrene/divinylbenzene-based ion-exchange material (top) and its structural representation (bottom).	62
3.2	A popular chemical structure of two perfluorinated ion-exchange materials (Na^+ can be replaced by other cations) and their structural illustration (bottom). (From Davis, T. A. et al. 1997. <i>A First Course in Ion Permeable Membranes</i> . Electrochemical consultancy; Gierke, T. D. et al. 1982. <i>ACS Symp. Ser.</i> 180:195–216; and Asahi Chemical Industry Co., LTD. 1995. Aciplex formula. Public release.)	64
3.3	Illustration of the cation polymer showing fixed ionic groups (SO_3^-), counter-ions (Li^+), and co-ions (y^-), respectively.	65
3.4	Experimental setup used.	67
3.5	Absorption isotherms of Nafion™.	67
3.6	Enthalpy of H_2O absorption as a function of the water content (Nafion). (Escoubes, M. and M. Pineri. 1982. In <i>Perfluorinate Ionomer Membranes</i> , ed. A. Eisenberg and H. L. Yeager. Washington, D.C.: American Chemical Society.)	68
3.7	DSC data for cooling of Nafion (Li^+ form). (Yoshida, H. and Y. Miura. 1992. <i>J. Membrane Sci.</i> 68:1–10.)	68
3.8	Number of water molecules per an ionic group in Nafion (Li^+ form). The total number of water molecules is 19.6. (Davis, T. A. et al. 1997. <i>A First Course in Ion Permeable Membranes</i> . Electrochemical consultancy.)	69

Figure	Description	Page
3.9	Two schematic diagrams showing different preparation processes. Top left: A schematic shows initial compositing process; top right: its top-view SEM micrograph. Bottom left: A schematic shows surface electroding process; bottom right: its top-view SEM micrograph where platinum is deposited predominantly on top of the initial Pt layer.	70
3.10	TEM micrographs show a cross-section of an IPMNC (left) and its close-up (right).	71
3.11	TEM successive micrographs showing the platinum particles reduced within the polymer matrix as well as typical nanoparticles of platinum.	72
3.12	Various surface micrographs of IPMNCs using different techniques of chemical plating and placing electrodes on the boundary surfaces.	73
3.13	A cross-section of an IPMNC showing two electrodes (top and bottom) with porous expanded graphite and dense platinum. This IPMNC is manufactured by the solution-casting and further treatment with porous graphite and chemical reduction of platinum as effective compliant electrodes.	74
3.14	S/N response graphs for factors A through F.	77
3.15	S/N response graphs for factors G through L.	78
3.16	S/N response graph for factor M.	79
3.17	A comparison of blocking forces for 29 different Taguchi samples.	80
3.18	Four-point probe surface resistivity measurement on Taguchi samples. (Shahinpoor, M. and K. J. Kim. 2001. <i>Smart Mater. Struct. Int. J.</i> 10:819–833.)	81
3.19(a)	Tensile testing results for Taguchi samples 1, 2, and 3. Also, Nafion-117, H+ form, both dry and wet, is shown.	82
3.19(b)	Tensile testing results for Taguchi samples 28 and 29. Also, Nafion-117, H+ form, both dry and wet, is shown.	82
3.20	Current responses to step voltages of 1, 2, 3, and 4 V for Taguchi sample 3.	83
3.21	Current responses to step voltages of 1, 2, 3, and 4 V for Taguchi sample 28.	84
3.22	Effects of various cations on the actuation of the IPMNC muscle. Comparisons were made against Na+ in terms of maximum force generated at zero displacement. A sinusoidal input voltage of 1.2 V _{rms} and a frequency of 0.5 Hz were set for all experiments. The samples were cut in a standard size of 0.675 × 2.54 cm. Na+ was chosen as a reference since it is coordinated with four water molecules.	85
3.23	The specific force generated per an applied input power by the ERI-S1 IPMNC.	86
3.24	Force generated by an IPMNC with respect to time in minutes. The measured force under a step voltage of 1.2 V clearly shows nearly no decay in the force generated over a period of 2 min. The dimension of the IPMNC sample is 0.25 × 0.75 in. In this case, the surface electrode is effectively made to block water leakage (organic ions were incorporated as well).	86
3.25	Force response characteristics of the IPMNC under different voltage wave forms.	87
3.26(a)	Power consumption of IPMNC versus time. Note that the platinum reduction was completed five times and final electroplating was done with gold. Also, phase shifts can be seen as the platings proceed.	88
3.26(b)	Current/voltage characteristics of IPMNC. Note that the platinum reduction was completed five times and final electroplating was done with gold. Also, phase shifts can be seen as the platings proceed.	88
3.27(a)	An SEM cross-section (top) of the sample and its surface (bottom), respectively. The cross-sectional view shows two platinum penetration leading edges and gold surface electrodes. The surface is fairly uniform but shows minor imperfect spots.	89

Figure	Description	Page
3.27(b)	A schematic showing how the loose and ion-hydrated water is gushing out under an imposed voltage.	90
3.28(a)	SEM micrographs showing surface morphologies of the IPMNC sample without the use of a dispersing agent.	91
3.28(b)	SEM micrographs showing surface morphologies of the IPMNC sample with the use of a dispersing agent.	91
3.29	Comparisons of six different IPMNC samples treated with dispersing agents.	92
3.30	Platinum reducing process. Dark circles represent platinum particles.	92
3.31	Platinum particle geometry and distributions before (left) and after (right) stretching 17% uniaxially.	93
3.32	Change in blocking force for typical samples after stretching.	93
3.33	Change in blocking force for typical samples after stretching.	94
3.34	Change in blocking force for typical samples after stretching. The force is increased by a factor of almost two.	94
3.35	Additional data for increase in blocking force for typical samples after stretching.	95
3.36	Additional data for increase in blocking force for typical samples after stretching.	96
3.37	SEM of 4% stretched IPMNC samples.	96
3.38	SEM of 5% stretched IPMNC samples.	97
3.39	SEM of 17% stretched IPMNC samples.	97
3.40	SEM of 17% stretched IPMNC samples (close-up).	97
3.41	SEM micrograph of a stretched IPMNC (19% stretching) and its force performance. Note that an additive, PVP, was added.	98
3.42	Concentration of Pt-Pd particles during chemical plating at a certain depth away from the surface of IPMNCs.	99
3.43	Measured blocking forces (top) and surface resistance of IPMNC samples prepared (bottom). The standard sample size is $5 \times 10 \times 0.2$ mm. The process information is given in terms of particles used, platinum, and the final electroded material, gold.	100
3.44	Typical AC impedance data on an IPMNC.	101
3.45	A typical set of data shows the voltage, E , drop along the surface-electrode direction, L .	101
3.46	A schematic diagram of the typical silver- (or copper-) deposited IPMNC artificial muscle fabricated.	102
3.47	The measured platinum concentration profile (top) and a typical x-ray spectrum (bottom).	102
3.48	An atomic force microscopy image taken on the surface electrode of a typical muscle shown in figure 3.8. The scanned area is $1 \mu\text{m}^2$. The brighter/darker area corresponds to a peak/valley depth of 50 nm. The surface analysis image has a view angle set at 22° .	103
3.49	A schematic diagram illustrating the silver deposition process (left) along with a typical x-ray spectrum taken on the surface. Low voltage was applied to carry out the silver deposition.	104
3.50	The IMPC artificial muscle response for sinusoidal wave input at $2 V_{\text{rms}}$. Tests were performed in air and without preloading.	105
3.51	The measured surface resistance of the samples prepared in this study (a) and the ratio of the measured maximum force of samples 2 and 3 relative to sample 1. The effective length, l_{eff} , was set at 20 mm for all samples.	106
3.52	The current responses of IPMNC muscles (sample 1 vs. sample 2). A step voltage of 2.2 V was applied.	107

Figure	Description	Page
3.53	A schematic process illustration of the PLI-IPMNCs (left) and silver particle used (right). (Shahinpoor, M. and K. J. Kim. 2002. In <i>Proceedings of SPIE 9th annual international symposium on smart structures and materials</i> . SPIE publication no. 4695, paper no. 36.)	108
3.54	SEM micrograph of IPMNC and (a) its close-up and (b) x-ray line scan (c), respectively. The silver penetration is about 7–8 μm for this sample and the majority of silver particulates are in tack within the ion-exchange polymer.	109
3.55	SEM micrograph showing Ag surface properly electroded and composited on to an ion-exchange polymer.	109
3.56	Force response characteristics of the IPMNC made by the physically loaded technique (top: 1-V responses and bottom: 1.5-V responses, respectively). The blocking force, F_b , was measured at the tip of the cantilever configuration with slightly preloaded conditions of 0.27 and 0.32 g, respectively.	110
3.57	Various IPMNCs with three-dimensional shapes.	112
3.58	The IPMNCs made with solution recast Nafion. Top two photos show the fabricated eight-finger IPMNC (<i>Octopus-IPMNC</i>). It (2-mm thickness) can easily sustain the eight U.S. quarters. (Note that a U.S. quarter has a mass of 5.3 g.) The diameter of this IPMNC is approximately 10.5 cm. The electrode is centered. The middle and bottom photographs show the IPMNC in action without applying load and with a load. As can be seen, a quarter is lifted. The time interval between the frames is approximately 1 sec. A step voltage of 2.8 V was applied ($E = 1.4$ V/mm). These IPMNCs were manufactured by typical metal-reducing techniques. Platinum was composited initially and gold was plated later. The cation is Li^+ .	113
3.59	An illustrative process diagram for the ion-conducting, powder-coated electrode made by the solution recasting method. First, the ion-conducting powder (i.e., carbon, silver, platinum, palladium, gold, copper, and any other conducting powders) is mixed with the electroactive polymer solution (e.g., liquid Nafion). The powder is fine and uniformly dispersed within the electroactive polymer solution. After a formation of a thin layer, the electroactive polymer solution undergoes the drying process of solvents and therefore the residual consists of the ion-conducting powder dispersed within the polymer. Second, the electroactive polymer solution (without the powder) is added on top of the layer of the ion-conducting powder and dried. This is repeated until the desired thickness is obtained. Later, a layer of the ion-conducting powder is formed by the same method described previously. As a final step, the ion-conducting, powder-coated electrode is cured under the elevated temperature. If necessary, the surface conductivity can be enhanced by adding a thin layer of novel metal via electroplating or electroless plating.	114
3.60	Tensile testing results (normal stress, σ_N , vs. normal strain, ϵ_N). Note that both samples were fully hydrated when they were tested. (a) Solution recast membrane; (b) as-received membrane.	115
3.61	Force responses of the solution recast IPMNC sample (top) and its conjugated graph showing tip displacement δ_T versus blocking force, F_T (bottom). Note that the frequency is 0.5 Hz and step voltages of 2, 4, and 6 V were applied.	116
3.62	Thermodynamic efficiency of the IPMNC as a function of frequency.	117
3.63	Force characteristics and input power consumptions of IPMNCs (conventional IPMNC and pyrrole-treated IPMNC). Polymerization of pyrrole was carried with the presence of a catalyst within the base polymer Nafion.	118

Figure	Description	Page
4.1	Assortment of pH muscles made from PAN fibers. Clockwise from left: encapsulated biceps muscle, triceps muscle, linear fiber bundle, linear platform muscle, encapsulated fiber bundle, and parallel fiber muscles.	121
4.2	Two PAN muscles (50-fiber bundles) encapsulated with latex membrane incorporating three-way glass fittings at each end to allow for the transport of pH solutions within the fiber bundles (relaxed length is 3 in.).	121
4.3	Single 100-fiber bundle encapsulated PAN muscle with three-way fittings designed especially for transport of pH solution and water within the fiber bundle (relaxed length is 6 in.).	122
4.4	Isotonic (left) and isoionic (right) test fixtures for PAN fiber artificial muscles.	123
4.5	Schematic diagram of the isoionic test fixture.	123
4.6	Isoionic test fixture shown with a 25-fiber bundle PAN muscle.	124
4.7	PAN (before activation) heated at 220°C for 1 h, 15 min.	125
4.8	Annealed PAN (close-up).	125
4.9	Annealed PAN, a single fiber (close-up). Its surface shows a texture that is believed to be an oxidized state of the fiber.	125
4.10	Activated PAN at a low-pH condition (1 N HCl).	126
4.11	Activated PAN at a low-pH condition (1 N HCl).	126
4.12	Activated PAN at a low-pH condition (1 N HCl).	126
4.13	Activated PAN at a low-pH condition (1 N HCl).	127
4.14	Activated PAN at a high-pH condition (1 N NaOH).	127
4.15	Activated PAN at a high-pH condition (1 N NaOH).	128
4.16	Activated PAN at a high-pH condition (1 N NaOH).	128
4.17	Activated PAN at a high-pH condition (1 N NaOH).	128
4.18	Activated PAN at a high-pH condition (1 N NaOH) (close-up).	129
4.19	Activated PAN at a high-pH condition (1 N NaOH).	129
4.20	Raw nano-PAN fibers.	129
4.21	Raw nano-PAN fibers (close-up).	130
4.22	Activated nano-PAN at a low-pH condition (1 N HCl).	130
4.23	Activated nano-PAN at a low-pH condition (1 N HCl) (close-up).	131
4.24	Activated nano-PAN at a high-pH condition (1 N NaOH).	131
4.25	Activated nano-PAN at a high-pH condition (1 N NaOH) (close-up).	132
4.26	PAN fiber length change (lithium hydroxide and HCl).	132
4.27	PAN fiber length change (potassium hydroxide and HCl).	132
4.28	PAN fiber length change (sodium hydroxide and HCl).	133
4.29	PAN elongation behavior explained by the osmotic behavior.	133
4.30	Thin wires used as effective spring electrode.	134
4.31	A PAN electrification configuration using a thin wire electrode and countermembrane electrode.	134
4.32	Photographs of experimental setup.	138
4.33	Electric activation of PAN fibers (LiOH) in NaCl.	139
4.34	Electric activation of PAN fibers (LiOH) in NaOH.	140
4.35	Electric activation of PAN fibers (NaOH) in NaCl.	141
4.36	A PAN electrification configuration using a thin wire electrode and countermembrane electrode.	141
4.37	PAN actuator system design.	142
4.38	Rubber boots.	142
4.39	Spring electrodes. Left: uncoated; right: gold coated.	143

Figure	Description	Page
4.40	Results of LiOH PAN activated in 0.1 <i>N</i> HCl.	144
4.41	Previous results of LiOH PAN activated in 0.1 <i>N</i> NaCl.	145
4.42	Electrical activation of real (pure) PAN fibers in 0.1 <i>N</i> NaCl.	145
4.43	Electrical activation of regular PAN fibers in 0.1 <i>N</i> NaCl.	146
4.44	PAN film cast after cross-linking.	146
4.45	A concept drawing of PAN muscle system (left) and fabricated model (right).	146
4.46	Annealed (cross-linked) PAN fibers.	147
4.47	Looped PAN fiber bundle.	147
4.48	Bottom and top caps. The bottom cap (left) places a magnetic stirrer that stirs the solution during the electric polarity change.	148
4.49	Revised design of PAN muscle system (left) and a fabricated model (right).	149
4.50	Raw PAN fiber (left) and activated PAN fiber (right).	149
4.51	A PAN muscle system under an electric field: initial (left) and after 15 min (right).	150
4.52	PAN fiber displacement in a HCl solution (1 <i>M</i>): initial (left) and after 15 min (right) positions.	150
4.53	Horizontal self-powered pH meter equipped with PAN fibrous muscle fibers and a resilient rotating cylinder.	150
4.54	Vertical self-powered pH meters equipped with PAN fibrous artificial muscles and a resilient rotating cylinder.	151
4.55	Vertical pH meter assembly made from a parallel type PAN fiber muscle and a specially designed container holding the fluid with unknown pH to be determined.	151
4.56	Linear pH meter using a graduated cylinder with calibrated PAN fiber bundle.	152
4.57	Circulatory system assembly pumping pH solutions into a biceps PAN artificial muscle.	153
4.58	PAN biceps muscle shown in a test apparatus consisting of a multichannel pump, microcontroller board, solenoid valves, and a desktop PC to activate a skeletal forearm.	153
4.59	Close-up of the attachment of the fabricated biceps PAN muscle on a life-size human forearm skeleton showing the controller board housed in the pelvic bone area and solenoid valves attached to the humerus and ulna bones, respectively. We also designed and built a simple pH meter with PAN fiber bundles using the parallel type packaging of the fibers as shown earlier (fig. 4.55). The picture shown is a rotary-type pH meter taking up a small space and fairly accurate for most cases.	154
4.60	Linear platform actuator for use in robotics.	154
4.61	Electric PAN muscle apparatus showing gold-plated center rod as one electrode and gold-plated spring as the circumferential electrode.	155
4.62	Exploded view of the electric PAN muscle apparatus.	156
4.63	A number of early contractile synthetic chemomechanical muscles.	157
4.64	A possible configuration for the electroactive C-PAN-N artificial muscle in an antagonist configuration to provide biceps and triceps (left) similar to the action of a sarcomere (right).	158
4.65	Normal stress–strain relationship for the contracted and the expanded state of PAN muscles.	160
4.66	Possible structure of activated polyacrylonitrile.	160
4.67	SEM micrographs that show raw fibers (top left), contracted (top right), and elongated states (bottom right), respectively. It should be noted that SEM micrographs were taken for the dry samples. The elongated PAN fibers show that they contain a salt (possibly NaCl).	161

Figure	Description	Page
4.68	Experimental setup for electrical activation of C-PAN artificial sarcomeres and muscles. It describes the operating principle of the C-PAN.	162
4.69	Electrical activation of muscle made up of fiber bundle of 50 C-PAN platinum fibers. Initial muscle length = 5.0 cm; number of fibers = 50; cell voltage = 20 V; current = 120 mA. Polarity of electrodes reversed at $t = 10$ min.	163
4.70	SEM micrograph shows platinum delamination over a number of cycles (right).	163
4.71	SEM micrograph shows the graphite fibers used in this study (left). Each fiber has a diameter of 6.4 μm and the configuration of the graphite electrode and PAN muscle (right).	164
4.72	Variation of length of 100 C-PAN-G fibers in fiber bundle form with time in a 0.2-mN NaCl cell under an imposed electric field (1PAN-2G ratio, 100 fibers).	165
4.73	Variation of length of PAN-graphite muscle with time in a 0.2-mN NaCl cell under a voltage of 20 V (1PAN-2G ratio, 50 fibers).	165
4.74	Electrical activation of C-PAN made with single PAN graphite fibers of 2,000 strands.	166
4.75	Variation of length of C-PAN-G strands of 10 μm in diameter with time in a 0.2-mN NaCl cell under a voltage of 20 V (1PAN-2G ratio in a special helically wound configuration).	166
4.76	Conventional PAN fibers. The fiber diameter is 8–10 μm .	167
4.77	Spun PAN nanofibers. Average fiber diameter is approximately 300–600 nm.	167
4.78	PAN elongation behavior explained by the osmotic behavior and PAN fibers in different states. Top left: neutral state; top right: under alkaline solutions. Therefore, if pure water is in contact with alkaline PAN, there will be an osmotic pressure driven water in flux. Bottom left: oxidized PANs (prior to activation); bottom middle: at low pH, contracted PAN (1 N HCl); bottom right: at high pH, expanded PAN (1 N LiOH).	168
4.79	Raw PAN fibers.	169
4.80	After oxidation (cross-linked)—before activation.	169
4.81	Spun PAN nanofibers. (a) A Phillips XL30 ESEM using an accelerating voltage of 10 kV was employed to take this SEM photograph; (b) ESEM image of the polyacrylonitrile nanofibers spun at 1 kV/cm; (c) PAN nanofibers (~300 nm diameter). Hitachi 4700 was used (an acceleration voltage of 3 kV).	170
4.82	NMR spectrum of PAN processed fibers.	171
4.83	Schematic of the electrospinning process.	172
4.84	Photographs of viscous polymer solution suspended at a capillary tip with (a) no applied potential and (b) just above the critical voltage.	173
4.85	A PAN actuator system.	174
4.86	The exchange of counter-ions and surrounding solvent.	175
4.87	Experimental setup for electrical activation of PAN fibers.	179
4.88	Previous (left) and new (right) PAN actuating systems.	180
4.89	Erosion of the electrode used after the operation.	181
4.90	The new PAN system produced a 5-mm displacement (a generative force of 50 gf).	181
4.91	An expanded state of the PAN fiber.	183
4.92	An electrically induced, contracted state of the PAN fiber.	183
4.93	A chemically induced, contracted state of PAN fiber (at 2 N HCl).	183
4.94	A micrograph of a PAN raw fiber.	184
4.95	A micrograph of an oxy-PAN (after heat treatment).	184
4.96	Braided PAN bundle in an expanded state.	185

Figure	Description	Page
4.97	Dimensional changes of the electrochemical cell system.	185
4.98(a)	Straight PAN fiber bundle muscle with end hooks.	186
4.98(b)	Looped PAN muscle.	186
4.99	Braided PAN fiber actuator test: initial (left) and after 25 min (right).	186
4.100	Spring for small-scale PAN fiber test.	187
4.101	Small-scale PAN fiber test with resilient springs.	187
4.102	A fabricated small-scale PAN system.	188
4.103	Initial length (left) and contracted length (right).	188
4.104	Force with time variations. Acid activated: baseline condition (actuated at pH of 1 N HCl); E-activated2: sample 1 electrically actuated; E-activated1: sample 2 electrically actuated.	189
4.105	Load cell setup to measure the generative force of PAN muscle (top). Single PAN fiber adhered to two screw bolts before test (bottom left) and after test (bottom right).	190
4.106	The modified test setup (left) and fiber bundle (right).	190
4.107	Force generation depending upon time with voltage change.	191
4.108	Force changes from switching polarity.	192
4.109	Load cell sensor to measure the force of PAN muscle: front view (left) and side view (right).	192
4.110	Single fiber force curve under 5-V electric field.	193
4.111	PAN fiber length (before test: 170 mm [left]; after test 165 mm [right]), under 5 V.	193
4.112	PAN fiber length (before test: 175 mm [left]; after test: 170 mm [right], under 7 V.	194
4.113	Force, current, and temperature versus time, under 7 V.	195
4.114	Force, current, and temperature versus time, under 5 V.	196
4.115	Force generation depending upon time, under 3 V.	197
4.116	Force changes from switching polarity.	198
4.117	Force versus displacement, under 7 V.	198
4.118	Force versus displacement, under 5 V.	199
4.119	Computer simulation (solid lines) and experimental results (scattered points) for the time profiles of relative weight of the gel sample for various degrees of swelling q .	202
4.120	Experimental result taken from direct measurement of a sample PAMPS muscle. (Gong, J. P. and Y. Osada. 1994. In preprints of the <i>Sapporo symposium on intelligent polymer gels</i> , 21–22; Gong, J. et al. 1994. In <i>Proceedings of the international conference on intelligent materials</i> , 556–564.)	202
4.121	Woven fabric forms of PAN muscles.	203
4.122	Electrochemical test setup.	204
4.123(a)	Force versus time curve with 0.01 M HCl.	205
4.123(b)	Force versus time curve with 0.01 M HCl.	205
4.124(a)	Force versus time curve with 0.5 M HCl.	205
4.124(b)	Force versus time curve with 1 M HCl.	206
4.125	Force versus time curve with 2 M HCl.	206
4.126	Force curve under 0.01 N of HNO_3 (left) and H_2SO_4 (right).	207
4.127	Force curve under 0.1 N of HNO_3 (left) and H_2SO_4 (right).	207
4.128	Force curve under 0.5 N of HNO_3 (left) and H_2SO_4 (right).	208
4.129	Force curve under 0.5 N of HNO_3 (left) and H_2SO_4 (right).	208
4.130	Fatigue confirmation test with 1 N HCl (left) and 1 N HNO_3 (right) after sulfuric and nitric acid test.	208
4.131	Single PAN fiber tensile machine setup.	209

Figure	Description	Page
4.132	New electrodes for anode (left) and cathode (right).	209
4.133	Test apparatus for new electrodes.	210
4.134	New electrodes for anode (left) and cathode (right).	210
4.135	Force generation by HCl 2 M (left) versus 5-V electric field (right).	211
4.136	Dimensions of the robotic finger.	212
4.137	Schematics of PAN muscle hand, original position (upper) and in grab motion (bottom).	212
4.138	Initial position of a single PAN finger.	213
4.139	Grab position performance of a single PAN finger.	213
4.140	PAN fiber bundle muscles in action as a single finger.	214
4.141(a)	Frontal view of PAN five-fingered hand.	215
4.141(b)	Back view of PAN five-fingered hand.	215
4.142(a)	Left side view of PAN five-fingered hand.	215
4.142(b)	Right side view of PAN five-fingered hand.	216
4.143	Five-fingered hand drawings.	217
4.144	Stress-strain curve of elongation and contraction state of single PAN fiber.	218
4.145	(a) A typical setup for a PAN fiber bundle; (b) Oxidation or contracted mode of a PAN fiber bundle; (c) Reduction or expanded mode of a PAN fiber bundle.	219
4.146	Minute PAN fiber change before (left) and after (right) applying 1 M HCl solution.	219
5.1	PAMPS muscle shown in bent state after applying a 30-V DC field. There are two gold-plated electrodes at each side of the Teflon (polytetrafluoroethylene, PTFE) container.	225
5.2	Deformation of PAMPS ionic gel cylinder due to an imposed radial voltage gradient.	226
5.3	A possible charge redistribution configuration in ionic gels.	227
5.4	Experimental setup for electrically activated optical lens.	231
5.5	Stretching of the swollen zone due to electric field.	231
5.6	Observed deformation of the gel lens under the influence of the electric field.	231
5.7	Actual experimental observation on the deformation of adaptive optical lens under electrical control. (From Salehpoor, M. et al. 1996. In <i>Proceedings of the SPIE conference on intelligent structures and materials</i> , 2716:36–45.)	232
5.8	Experimental setup for measuring the focal length of the gel lens.	232
5.9	Robotic swimming structure (top) and swimmer with muscle undulation frequency of 3 Hz (bottom). The scale shown is in centimeters.	233
6.1	Gel disk swelling problem.	245
6.2	Finite element mesh on gel geometry.	245
6.3	Outer edge radial displacement as a function of time.	246
6.4	Solvent mass fraction at time = 20 sec.	246
6.5	Solvent mass fraction at time = 200 sec.	247
6.6	Solvent mass fraction at time = 500 sec.	247
6.7	Pressure at time = 20 sec.	248
6.8	Pressure at time = 200 sec.	248
6.9	Pressure at time = 500 sec.	249
6.10	Bending of an ionic gel strip due to an imposed electric field gradient.	250
6.11	Geometry of microbending for an elastic strip of ionic gels.	251
6.12	A possible charge redistribution configuration in ionic gels.	253
6.13	Variation of curvature versus cross-capacitance C_g and time t .	261
6.14	Variation of curvature versus cross-resistance R_g and time t .	261
6.15	Variation of curvature versus cross-electric field E and time t .	262

Figure	Description	Page
6.16	Variation of maximum tip deflection δ_{\max} versus average cross-capacitance C_g and time t .	262
6.17	Variation of maximum tip deflection δ_{\max} versus the average electric field E and time t .	263
6.18	Variation of maximum tip deflection δ_{\max} versus average cross-resistance R_g and time t .	263
6.19	Computer simulation (solid lines) and experimental results (scattered points) for the time profiles of relative weight of the gel sample for various degrees of swelling, q .	267
6.20	Numerical simulation of equation 6.89 by Asaka and Oguro (Asaka, K. and K. Oguro. 2000. <i>J. Electroanalytical Chem.</i> 480:186–198.)	268
6.21	Spatial geometry of a local polymer segment with fixed charges.	270
6.22	Nonuniform distribution of Coulomb's forces along the gel axis.	272
6.23	The simplest solution for a configuration with a few cations before activation.	272
6.24	The simplest solution for a configuration with a few cations after activation.	273
6.25	Force improvement by chemical tweaking showing the effect of changing cations from H^+ to Na^+ to Li^+ .	276
6.26	Experimental evidence for the effect of different ions and their hydration numbers on the tip force and thus deformation of an IPMNC strip.	276
6.27	General structures of an IPMNC or IPCNC film with near-boundary functionally graded electrodes and surface electrodes.	279
6.28	Schematics of the electro-osmotic migration of hydrated counter-ions within the IPMNC network.	280
6.29	Dynamic sensing of the ionic polymer due to imposed deformation.	281
6.30	Actuation under a low-frequency electric field to minimize the effect of loose water back diffusion.	282
6.31	Experimental determination of Onsager coefficient L using three different samples.	283
6.32	Deflection under a step voltage for fully hydrated and semidry samples. Note a small back relaxation due to presence of loose water (a) and virtually no back relaxation due to absence of loose water (b).	284
6.33	Displacement characteristics of an IPMNC, Tokuyama Neosepta CMX (styrene/divinylbenzene-based polymer). δ : arc length; L_o : effective beam length; $L_o = 1.0$ in. (top) and 1.5 in. (bottom).	285
6.34	Displacement characteristics of an IPMNC, ERI-S1. δ : arc length; L_o : effective beam length; $L_o = 1.0$ in. (top) and 1.5 in. (bottom).	286
6.35	Typical deformation of strips ($10 \times 80 \times 0.34$ mm) of ionic polymers under a step voltage of 4 V.	286
7.1	Successive photographs of an IPMNC strip that shows very large deformation (up to 4 cm) in the presence of low voltage. The sample is 1 cm wide, 4 cm long, and 0.2 mm thick. The time interval is 1 sec. The actuation voltage is 2 V DC.	294
7.2	A typical sensing response of an IPMNC. The IPMNC ($5 \times 20 \times 0.2$ mm) in a cantilever mode as depicted in figure 7.1 is connected to an oscilloscope and is manually flipped to vibrate and come to rest by vibrational damping.	295
7.3	The measured AC impedance characteristics of an IPMNC sample (dimension = 5-mm width, 20-mm length, and 0.2-mm thickness).	296
7.4	An equivalent electronic circuit for a typical IPMNC strip obtained by an impedance analyzer.	297

Figure	Description	Page
7.5	Measured surface resistance, R_s , of a typical IPMNC strip, as a function of platinum particle penetration depth.	297
7.6	The current, $i(t)$, versus $t^{-1/2}$ (chronoamperometry data). Note that $A = 6.45 \text{ cm}^2$ and $E = -3 \text{ V}$.	298
7.7	Equivalent circuit model representing an IPMNC.	299
7.8	An SEM micrograph shows the cross-section of an IPMNC sensor. It depicts a cross-section (left) of an IPMNC strip, its close-up (right), and the x-ray line scan (bottom).	300
7.9	DC sensing data in terms of produced voltages, ΔE , versus displacement. Note that the displacement is shown in terms of the deformed angle relative to standing position in degree. The dimension of the sample sensor is $5 \times 25 \times 0.12 \text{ mm}$.	301
7.10	Accelerometer implementations using PZT in (a) 3–3 mode and (b) 3–1 mode.	302
7.11	Dry IPMNC impedance magnitude.	304
7.12	Dry IPMNC impedance phase.	305
7.13	Wet IPMNC impedance magnitude.	305
7.14	Wet IPMNC impedance phase.	306
7.15	PZT frequency response magnitude.	306
7.16	IPMNC frequency response magnitude.	307
7.17	Typical voltage/current output (a) and power output (b) of IPMNC samples.	309
7.18	Outvoltage due to normal impact of 200-N load on a $2\text{-cm} \times 2\text{-cm} \times 0.2\text{-mm}$ IPMNC sample.	310
7.19	IPMNC cantilever beam.	310
7.20	Simulink model.	312
7.21	Hypothetical deflection plot.	312
7.22	Beam “lengthening.”	313
7.23	Segmented beam.	313
7.24	Unstretched hypothetical deflection plot.	314
7.25	Deflections due to various moments.	314
7.26	Beam tip step response.	315
7.27	Beam modeling process.	315
7.28	Time history of beam deflection.	317
7.29	“Flapping” beam.	317
7.30	Moment induced by electric field.	318
7.31	Hypothetical moment simplification.	318
7.32	Tip displacement of IPMNC actuator for 1 V.	319
7.33	Experimental closed-loop tip response for $10\text{-} \times 20\text{-mm}$ IPMNC actuator for a step voltage of 1 V.	320
7.34	(a) Fixture for impedance test; (b) Impedance analyzer.	320
7.35	Measured impedance at an input voltage of 0.5 V.	321
7.36	Phase of the electromechanical impedance at 0.5 V.	322
8.1	Simple structures of polyacetylene alternating single and double bonds between carbon atoms.	323
8.2	Molecular structure of a simple polypyrrole conductive polymer.	323
8.3	Sketch representing a REDOX reaction of PPy due to the presence of ionic ClO_4^- anions.	325
8.4	REDOX cycle of PANi in HCl aqueous solution. The emeraldine salt is oxidized into pernigraniline (PS) salt or reduced into leuco-emeraldine (LS) salt. (Tourillon, G. and F. Garnier. 1984. <i>J. Electroanal. Chem.</i> 161:51.)	327

Figure	Description	Page
8.5	Picture showing the actuation mechanism of a molecular actuator based on PT chains interconnected with a highly versatile molecule as a calixarene. (Anquetil, P. A. et al. 2002. In <i>Proceedings of SPIE smart structures and materials symposium</i> , 4695.)	328
9.1	The IPMNC gripper concept (top) and a four-finger gripper (bottom).	330
9.2	The three-dimensional IPMNC actuator concept.	331
9.3	The fabricated IPMNC in a square rod form.	332
9.4	The undulating and morphing actuator made with an IPMNC.	332
9.5	Robotic swimming structure (top) and swimmer with muscle undulation frequency of 3 Hz (bottom). The scale shown is in centimeters.	333
9.6	An illustrative design of robotic fish.	334
9.7	A robotic fish equipped with a single IPMNC tail fin.	334
9.8	A designed and fabricated undulating shark caudal fin actuator.	335
9.9	ERI's biomimetic fish with an emarginated type of caudal fin design.	335
9.10	Some typical naturally evolved designs for caudal fins.	336
9.11	Some natural designs for caudal fins.	336
9.12	Another ERI's biomimetic fish with an emarginated type of caudal fin design.	336
9.13	ERI's biomimetic fish with a shark type of caudal fin design.	337
9.14	An assortment of ERI's biomimetic robotic fish equipped with IPMNCs.	337
9.15	The newest generation of completely watertight and impermeable underwater biomimetic robotic fish equipped with IPMNCs.	338
9.16	A photograph of a platform actuator driven by eight IPMNCs (top). This design can feature two-dimensional motion of the platform. The operating principle is illustrated (bottom).	339
9.17	Assortment of bilinear and linear IPMNC actuators: a reference pair (top) and an activated pair (bottom).	339
9.18(a)	Schematics of an IPMNC cylindrical linear actuator with discretely arranged ring electrodes.	340
9.18(b)	Basic design configurations to make IPMNC linear actuators.	340
9.18(c)	Basic operational configurations of the IPMNC-based linear actuators.	340
9.18(d)	Basic electrode placement and configurations of the IPMNC-based linear actuators.	341
9.18(e)	Alternative design configurations of the IPMNC-based linear actuators.	341
9.18(f)	Operational configurations of the alternative design of IPMNC-based linear actuators.	341
9.18(g)	Laboratory prototype configurations of the IPMNC-based linear actuators.	342
9.18(h)	Another laboratory prototype of the IPMNC-based linear actuators.	342
9.18(i)	IPMNC-based linear actuator producing over 30% linear actuation.	342
9.19	Interdigitated electrode arrangement on an IPMNC strip to create a serpentine-like contractile and slithering artificial muscle.	343
9.20	Another interdigitated electrode arrangement on a slithering IPMNC strip to create a serpentine-like contractile and slithering artificial muscle.	343
9.21	Actual interdigitated electrode arrangement on a slithering IPMNC strip to create a serpentine-like contractile and slithering artificial muscle.	344
9.22	Metering valve data obtained by a strip of IPMNC undulating in a pipe flow.	344
9.23	A photograph of a fabricated double-diaphragm pump. The size of the IPMNC is 1-mm width \times 5-mm length \times 0.2-mm thickness.	345
9.24	Perspective view of two (rectangular and circular chamber) double-diaphragm minipumps equipped with IPMNC muscles and an inductive receiving coil.	345

Figure	Description	Page
9.25	Side view of the two double-diaphragm minipumps equipped with synthetic muscles and an inductive receiving coil.	345
9.26	Exploded view of the two double-diaphragm minipumps equipped with synthetic muscles and an inductive receiving coil.	346
9.27	Cutaway view of the double-diaphragm minipumps equipped with synthetic muscles and an inductive receiving coil.	346
9.28	A fabricated double-diaphragm minipump equipped with IPMNC diaphragms.	346
9.29	Human skeletal arm joints.	348
9.30	Human skeletal arm muscles.	349
9.31	(a) "Myster Bony," a plastic human skeleton equipped with electrically contractile muscle fabrics, riding an exercycle. (b) Schematic of an astronaut in a pressurized space suit equipped with joint power augmentation artificial muscles.	350
9.32	A photograph of a manufactured, micron-scale IPMNC that can be used for MEMS applications (top). Assembly of microstrips of IPPC cut in a laser-microscope work station for microsensing and microactuation (bottom).	354
9.33	Microgripper (a) and fabricated (b) designs.	355
9.34	Array of micro- and/or nanogrippers.	355
9.35	Various shapes of IPMNCs with three-dimensional shapes.	356
9.36	One-string musical instrument.	357
9.37	Data gloves with embedded IPMNC sensor elements.	357
9.38	General configuration for the proposed heart compression device.	358
9.39	Heart compression device equipped with IPMNC fingers.	359
9.40	A heart with an IPMNC compression band.	359
9.41	IPMNC compression bands in open and closed configurations.	360
9.42	Four-fingered heart compression device equipped with thick IPMNCs: (a) before compression; (b) after compression.	360
9.43	The upright configuration of the heart compression device.	360
9.44	Miniature heart compression device equipped with IPMNC muscles.	361
9.45(a)	Pressure generation versus electrode thickness.	361
9.45(b)	Pressure generation versus electrode thickness.	362
9.46	An artificial smooth muscle actuator that mimics a human hand (left) and a fabricated human joint mobility and power augmentation system equipped with IPMNCs (right).	363
9.47	The essential operation of the active scleral band to create bionic vision.	365
9.48	The eye in (a) is myopic (long and thus short sighted; image is formed inside the eye and does not reach the macula). The band expands the sclera outward to correct myopia (shortens the eye length and decreases corneal curvature) as in (b).	365
9.49	The eye in (a) is hyperopic (short and thus far sighted; image is formed outside and beyond the eye and does not reach the macula). The band contracts the sclera inward to correct hyperopia (increases the eye length and increases corneal curvature) as in (b).	365
9.50	Composite wing-flap made with IPMNCs.	366
9.51	An illustrative view of the IPMNC actuator showing a flying machine.	367
9.52	A fabricated IPMNC flying machine (top) and its resonance performance (bottom). Resonance was observed at about 7 Hz, where the associated displacement was observed approximately half of the cantilever length.	368
9.53	Possible wake capture mechanism.	368
9.54	A flapping wing system equipped with IPMNCs and the electronic driver.	369

Figure	Description	Page
9.55	Large arrays of undulating IPMNC strips acting like artificial coral reefs.	369
9.56	Another configuration of IPMNC artificial coral reefs.	369
9.57	Using IPMNCs in a platform type of configuration to create linear actuation.	370
9.58	IPMNC bending muscles (18) equipped with undulating optical fiber (14) for optical switching and light modulation.	370
A.1	Typical skeletal muscle showing epimysium, perimysium, and endomysium layers.	402
A.2	Motor unit showing two motor neurons supplying the muscle fibers.	403
A.3	Neuromuscular junction (NMJ).	403
A.4	Skeletal muscle structure.	405
A.5	Myofilament structure detail.	406
A.6	Sliding filament mechanism of muscle contraction.	407
A.7	Myogram of twitch contraction.	409
A.8	Length–tension relationship in skeletal muscle fiber.	411

Symbols

a	Maximum swelled distance from the center of the gel
B	Reduced electric potential
b	Polyion separation distance
b_i	Spacing between <i>i</i> th row of polyion segments
C	Total ion-exchange capacity, mL/g dry membrane; also, gel cylindrical sample half radial thickness
C_p	Power coefficient
C_T	Thrust coefficient
C_g	Specific capacitance of the gel, F/g
C_{mi}	Fourier coefficients
C_{oi}	Fourier coefficients
c_i	Concentration of the <i>i</i> th species
D	Dielectric constant of the liquid phase; also, drag force
D_{eff}	Effective diffusivity coefficient in cm ² /sec
D₀	Diameter of cylindrical polymer sample
ΔE	Driving force pumping ions; also, gradient of electric field
e	Electron charge, 1.602×10^{-19} C
E	Young's modulus
F	Total free energy; also, force performing mechanical work; also, force produced in the gel; also, mean coulomb attraction/repulsion forces associated with R^*
F₀	Force during isometric contraction
ΔF	Free energy decrease as a result of contact between two polymer networks
F_e	Free energy due to work done against electric field
F_g	Free energy due to gel deformation
f	Frequency, Hz; also, number of ionized segments out of N_0 total; also, friction coefficient between polymer network and liquid medium
G	Shear modulus
g	Local gravity acceleration, 9.81 m/s ²
H	Total amount of hydrogen ions (including undissociated)
h	Hydrogen ion concentration
\bar{h}	Hydrogen ion concentration inside the membrane
I	Electric current, A
i	Current density of the gel
K	Dissociation constant; also, modified Bessel function
k	Proportionality constant; also, Boltzmann constant, 1.381×10^{23} J/K; also, bulk elastic modulus of the gel polymeric component
L	Gel length when fully swollen
L₀	Length of cylindrical polymer sample

I	Uniaxial elongation of muscle fiber
N_0	Number of freely jointed segments of polymer
n	Number density of counter-ions; also, number of polyions
n_i	Number density of ions for the i th species
P	Pressure term, N/m^2 ; also, hydrostatic pressure term
pH	A measure of acidity or alkalinity of solution
Q	Electric charge, C; also, charge per unit mass or specific charge of the gel, C/g
q	Electric charge, C; also, degree of swelling
q_n	Quantity of mobile ions
R	Electric potential field per unit charge
R_+	Electric potential field corresponding to positive charges
R_-	Electric potential field corresponding to negative charges
R^*	Total electric field due to all strands of polymer network
R_g	Specific resistance of the gel, Ω/g
Re	Reynolds number
r	Hydrodynamic frictional coefficient; also, radius of ionic gel sample
r^*	Mean radius of ionic gel sample
r_i	Inner radius of elemental cylinder in gel fiber; also, cylindrical polar coordinate
r_o	Outer radius of elemental cylinder in gel fiber
S	Total amount of salt cation; also, entropy in thermodynamic context; also, wetted surface area in fluid mechanics
S_w	Linear swelling ratio
\underline{s}	Concentration of salt cation
\bar{s}	Concentration of salt cation inside the membrane
T	Absolute temperature, K; also, thrust force, N
t	Time, s
l^*	Thickness of gel cylindrical sample
U	Total internal energy, J; also, steady-state velocity term
u_0	Percent change of sample dimension at final state
u_{ij}	Displacement vector of the gel elemental volume from its position when the swelling process has gone to completion
V	Water volume; also, volume in thermodynamic sense; also, velocity of contraction
V_p	Volume of the dry polymer sample
V_T	Total volume
\bar{V}	Water volume inside the membrane
v	Voltage across the thickness of the gel, V
W	Dry weight of the muscle membrane or gel
w_0	Water content of the muscle membrane, ml/g
X	Total concentration (dissociated and undissociated) of weak acid groups in the membrane
Z	Distance of an element from free end of the gel; also, number of ionizable groups
Z_i	Cylindrical polar coordinate

ΔZ_0	Elemental disk thickness before applied electricity
z	Valance number
z_i	Valance of the i th species
α	Degree of dissociation; also, degree of ionization; also, factor increasing D_0 after application of electricity
β	Factor increasing ΔZ_0 after application of electricity; also, chemical stress term
β_m	Positive root of Bessel function of order zero
Γ	Modified Bessel function
Δ	Thickness term
δ_{ij}	Mechanical strain
ϵ	Dielectric constant; also, electric field energy; also, average electric charge
η	Fish propulsion efficiency
θ	Cylindrical polar coordinate angle
Φ	Contraction rate of the gel
ϕ	Volume fraction of the polymer network
ϕ_0	Concentration of polymer (no interaction between segments or reference states)
κ	Inverse of Debye length or effective thickness of the ionic layer surrounding the charge sites of the individual fibrils; also, phenomenological coefficient
λ	Dimensionless parameter relating to β
μ	Shear modulus; also, average mobility of the medium in the gel; also, solvent viscosity
μ_h, μ_s	Hydrogen-ion and salt-cation mobility
μ_i	Chemical potential (energy) for the i th species
ξ	Positive root of Bessel function of order zero
ρ	Density of liquid solvent
ρ^*	Charge density
σ_{ij}	Tensile stress, N/m ²
τ	Reduced temperature
ν	Number of polymers cross-linked in the network; also, velocity of contraction of the gel; also, three-dimensional liquid velocity vector
ψ	Local electrostatic potential

Acronyms

AMPS	2-Acrylamido-2-methyl-1-propanesulfonic acid monomer
CAM	Composite artificial muscles
DLVO	Combination double-layer forces and Van der Waals forces in ionic gels
HEMA	2-Hydroxyethyl methacrylate
IEM	Ion-exchange membrane
IEM-Pt	Ion-exchange membrane platinum
IEMMC	Ion-exchange membrane metal composite
IEMPC	Ion-exchange membrane platinum composite
IPCC	Ionic polymeric conductor composite
IPCNC	Ionic polymeric conductor nanocomposite
IPMC	Ionic polymeric metal composite
IPMNC	Ionic polymer-metal nanocomposite
MBAA	N, N'-Methylene- <i>bis</i> -acrylamide
PAAM	Polyacrylic acid <i>bis</i> -acrylamide
PAM	Polyacrylamide
PAMPS	Poly2-acrylamido-2-methyl-1-propanesulfonic acid
PAN	Polyacrylonitrile
PANi	Polyaniline
PPy	Polypyrrol

Contents

Chapter 1	Introduction to Ionic Polymers, Ionic Gels, and Artificial Muscles	1
1.1	Introduction	1
1.2	A Brief History of Electroactive Polymers (EAPs) and Artificial/ Synthetic Muscles	1
1.2.1	Electrically Conductive and Photonic Polymers	2
1.2.2	Magnetically Activated Polymers	2
1.2.3	Electronic EAPs/Ferroelectric Polymers	2
1.2.4	Electrets	3
1.2.5	Dielectric Elastomer EAPs	3
1.2.6	Liquid Crystal Elastomer (LCE) Materials	4
1.2.7	Ionic EAPs/Ionic Polymer Gels (IPGs).....	4
1.2.8	Nonionic Polymer Gels/EAPs	4
1.2.9	Ionic Polymer–Metal Composites (IPMNCs)	5
1.2.10	Conductive Polymers (CPs) or Synthetic Metals.....	5
1.2.11	Shape Memory Alloys (SMAs) and Small Memory Polymers (SMPs)	6
1.2.12	Metal Hydride Artificial Muscle Systems	6
1.2.13	Electrorheological (ER) Materials	7
1.2.14	Magnetorheological (MR) Materials	7
1.2.15	Magnetic Shape Memory (MSM) Materials	8
1.2.16	Giant Magnetostrictive Materials (GMMs).....	8
1.3	A Brief History of Electromotive Polymers.....	8
1.3.1	Contraction Behavior	17
1.3.2	Mechanisms.....	18
1.4	Role of Microparticles in Contraction of Gels	18
Chapter 2	Ionic Polymer–Metal Nanocomposites (IPMNCs): Fundamentals	23
2.1	Introduction	23
2.2	Performance Characteristics	32
2.2.1	Mechanical Performance	32
2.2.2	Electrical Performance.....	35
2.2.3	Improved Performance.....	39
2.2.4	A View from Linear Irreversible Thermodynamics	43
2.2.5	Thermodynamic Efficiency.....	44
2.2.6	Cryogenic Properties of IPMNC	48
2.2.7	Internal and External Circulatory Properties of IPCNCs	48

2.2.8	Near-DC Mechanical Sensing, Transduction, and Energy-Harvesting Capabilities of IPMNCs in Flexing, Bending, and Compression Modes	54
2.3	Advances in Force Optimization	56
2.4	Electric Deformation Memory Effects, Magnetic IPMNCs, and Self-Oscillatory Phenomena in Ionic Polymers	58
Chapter 3	Ionic Polymer–Metal Nanocomposites: Manufacturing Techniques	61
3.1	Introduction	61
3.2	IPMNC Base Materials	61
3.2.1	In General	61
3.2.2	Water Structure within the IPMNC Base Materials	66
3.3	Manufacturing Techniques	69
3.3.1	In General	69
3.3.2	IPMNC and IPCNC Manufacturing Recipe	71
3.3.3	Force Optimization	74
3.3.4	Effects of Different Cations	80
3.3.5	Electrode Particle Control	87
3.3.6	Additional Results on Stretched IPMNCs to Enhance Force Generation and Other Physical Properties	92
3.3.6.1	Platinum–Palladium New Phenomenon	95
3.3.7	Effective Surface Electrodes	98
3.3.8	An Economical Approach—Physical Metal Loading	106
3.3.9	Scaling	111
3.3.10	Technique of Making Heterogeneous IPMNC Composites	117
Chapter 4	Ionic Polyacrylonitrile Chemoelectromechanical Artificial Muscles/Nanomuscles	119
4.1	Introduction	119
4.2	PAN Fabrication	119
4.3	PAN Characterization	122
4.3.1	Isotonic Characterization	122
4.3.2	Isoionic Test	123
4.3.3	PAN Synthetic Muscles' Capability Measurements	124
4.3.3.1	SEM Studies	124
4.3.4	Effects of Different Cations	130
4.3.5	Electric Activation of PAN Fibers	133
4.3.6	Additional Results	133
4.3.7	Additional Experimental Results	138
4.3.7.1	Results	139
4.3.8	PAN Actuator System Design and Fabrication	142
4.3.9	PAN Performance Testing in an Acidic Environment	142
4.3.9.1	Procedures	143
4.3.9.2	Results	143

4.3.10	Pan Film Casting Experiment.....	143
4.3.11	PAN Actuator System Design and Fabrication	145
4.3.12	PAN Casting Experiment.....	147
4.3.13	Further PAN Actuator System Design and Fabrication	148
4.4	PAN pH Meters.....	149
4.4.1	Skeletal Muscles Made with Fibrous PAN Artificial Muscles	152
4.5	Electroactive PAN Muscles	153
4.6	Electrochemomechanical Actuation in Conductive Polyacrylonitrile (C-PAN) Fibers and Nanofibers	157
4.6.1	Introduction	157
4.6.2	Preparation of Ionically Active PAN.....	158
4.6.3	Direct Metal Deposition Technique.....	162
4.6.4	Graphite and Gold Fiber Electrode Woven into PAN Muscle as an Adjunct Electrode	164
4.6.5	Toward Nanoscaled Artificial Muscles and Motors	164
4.6.6	Experiment	168
4.6.7	Nanofiber Electrospinning in General.....	172
4.6.8	Fabrication of a PAN Actuator System	174
4.6.9	Contraction and Elongation Mechanism	175
4.6.10	Mathematical Modeling of Contraction and Elongation of C-PAN Fibers	176
4.6.10.1	Basic Modeling	176
4.6.10.2	Modeling	178
4.6.10.3	More Detailed Mathematical Modeling PAN Fiber Contraction/Expansion.....	178
4.6.10.4	PAN Actuator System Design and Fabrication.....	180
4.6.10.5	Further Modeling	182
4.6.10.6	PAN Actuator Fabrication.....	184
4.6.10.7	Additional Modeling.....	186
4.6.10.8	Small-Scale PAN Actuator Fabrication	187
4.6.10.9	Small-Scale PAN Actuator Fabrication and Testing	189
4.6.10.10	PAN Actuator System Testing	189
4.6.11	Electrocapillary Transport Modeling.....	194
4.6.12	Other Aspects of PAN Muscle Behavior.....	201
4.6.13	Force Generation with pH Difference	203
4.6.13.1	Mechanical Property of Single PAN Fiber	208
4.6.14	Effects of Electrode Deterioration on Force Generation	209
4.7	Five-Fingered Hand Design and Fabrication Using PAN Fiber Bundle Muscles.....	211
4.7.1	Fabrication of Five-Fingered Hand Equipped with Fiber Bundle PAN Muscles.....	213
4.7.2	Additional Mechanical Property Measurement of Single PAN Fiber.....	214
4.8	Micro-PAN Fiber Observation.....	216
4.9	Conclusions	216

Chapter 5	PAMPS Gel Artificial Muscles	221
5.1	Introduction	221
5.2	PAMPS Gels	223
5.3	Gel Preparation	223
5.4	PAMPS Gel Application	224
5.4.1	Adaptive Optical Lenses	224
5.4.2	Theoretical Model	225
5.4.3	Electrically Controllable Ionic Polymeric Gels as Adaptive Optical Lenses	229
5.4.4	Experimental Results: PAMPS	230
5.5	Electroactive PAMPS Gel Robotic Structures	232
5.6	Engineering Strength Considerations on PAMPS Gels	233
5.7	Gel Robotics	234
Chapter 6	Modeling and Simulation of IPMNCs as Distributed Biomimetic Nanosensors, Nanoactuators, Nanotransducers, and Artificial Muscles	237
6.1	Introduction	237
6.2	Continuum Electrodynamics of Ionic Polymeric Gels' Swelling and Deswelling	240
6.2.1	Basic Formulation	240
6.2.2	Computer Simulation of Symmetric Swelling and Contraction of Polyelectrolyte Gels	243
6.2.3	Gel Contraction/Shrinkage Example Based on the Continuum-Diffusion Model	244
6.3	Continuum-Diffusion Electromechanical Model for Asymmetric Bending of Ionic Polymeric Gels	248
6.3.1	Analytical Modeling	248
6.4	Continuum Microelectromechanical Models	262
6.4.1	Theoretical Modeling	262
6.4.2	Numerical Simulation	266
6.5	Microelectromechanical Modeling of Asymmetric Deformation of Ionic Gels	269
6.6	Time-Dependent Phenomenological Model	275
6.6.1	Two-Component Transport Model	275
6.6.2	Linear Irreversible Thermodynamic Modeling	279
6.6.2.1	Introduction	279
6.6.2.2	Steady-State Solutions	279
6.6.3	Expanded Ion Transport Modeling for Complex Multicomponent and Multicationic Systems and Ionic Networks	287
6.6.4	Equivalent Circuit Modeling	290
6.7	Conclusions	291

Chapter 7 Sensing, Transduction, Feedback Control, and Robotic Applications of Polymeric Artificial Muscles 293

7.1 Introduction 293

7.2 Sensing Capabilities of IPMNCs 293

7.2.1 Basics of Sensing and Transduction of IPMNCs and IPCNCs 294

7.2.2 Electrical Properties 295

7.2.3 Experiment and Discussion 299

7.3 Evaluation of IPMNCs for Use as Near-DC Mechanical Sensors 301

7.3.1 Introduction 301

7.3.2 Background 302

7.3.3 Experiment Setup 303

7.3.4 Experiment Results 304

7.3.5 Discussion and Conclusions 307

7.3.6 Advances in Sensing and Transduction 308

7.4 Simulation and Control of Ionoelastic Beam Dynamic

Deflection Model 308

7.4.1 Introduction 309

7.4.2 Static Deflection 310

7.4.3 Dynamic Case 313

7.4.4 Variable Moments 316

7.4.4.1 Moment Modification 316

7.4.4.2 Extension 317

7.4.4.3 Validation 318

7.4.5 Summary 318

7.4.6 Feedback Control in Bending Response of IPMNC Actuators 319

7.4.7 Results 320

7.4.8 Conclusions 322

Chapter 8 Conductive or Conjugated Polymers as Artificial Muscles 323

8.1 Introduction 323

8.2 Deformation of Conducting or Conjugated Polymers 324

Chapter 9 Engineering, Industrial, and Medical Applications of Ionic Polymer–Metal Nanocomposites 329

9.1 Introduction 329

9.2 Engineering and Industrial Applications 329

9.2.1 Mechanical Grippers 329

9.2.2 Three-Dimensional Actuator 330

9.2.3 Robotic Swimming Structure 331

9.2.4 Biomimetic Noiseless Swimming Robotic Fish 333

9.2.5 Linear Actuators 338

9.2.6	IPMNC Contractile Serpentine and Slithering Configurations.....	339
9.2.7	Metering Valves.....	343
9.2.8	Diaphragm Pumps Using Flexing IPMNC Strips and Diaphragms	343
9.2.8.1	Diaphragm Pump Designs.....	344
9.2.8.2	Exoskeletal Human Joint Power Augmentation (ESHPA)	348
9.2.9	Microelectromechanical Systems	349
9.2.10	Electromechanical Relay Switches.....	354
9.2.11	Continuous Variable Aperture Mirrors and Antenna Dishes.....	354
9.2.12	Slithering Device.....	356
9.2.13	Parts Orientation/Feeding	356
9.2.14	Musical Instruments.....	356
9.2.15	Flat Keyboards, Data Attire, and Braille Alphabet	356
9.3	Biomedical Applications	357
9.3.1	Artificial Ventricular or Cardiac-Assist Muscles.....	357
9.3.1.1	Electroactive Polymer-Powered Miniature Heart Compression Experiment	361
9.3.2	Surgical Tool	362
9.3.3	Peristaltic Pumps.....	362
9.3.4	Artificial Smooth Muscle Actuators	362
9.3.5	Artificial Sphincter and Ocular Muscles	364
9.3.6	Incontinence Assist Devices	364
9.3.7	Correction of Refractive Errors of the Human Eyes and Bionic Eyes and Vision.....	364
9.4	Aerospace Applications.....	366
9.4.1	Composite Wing-Flap	366
9.4.2	Resonant Flying Machine	366
9.4.2.1	Artificial Coral Reefs for Underwater Mine and Moving Object Detection	367
9.4.2.2	Other Uses	370
Chapter 10	Epilogue and Conclusions	371
10.1	Epilogue	371
10.2	Conclusions: PAN Muscles.....	372
10.3	Conclusion: IPMNC Actuators	372
10.4	Conclusion: IPMNC Sensors and Transducers	373
Appendix A	Anatomy and Physiology of Human Muscle	375
A.1	Muscle Contraction.....	380
A.2	Role of Structural Components of Muscle Fibers	385
A.3	Isotonic and Isometric Contraction	386
A.4	Skeletal Muscle Fiber Types.....	387

A.5 Electromyography 388

A.6 ATP 389

Appendix B Muscle Mechanics 391

References 395